ESI Supporting Information

Nanoparticles-in-Concavities as Efficient Nanocatalysts for Carbon Dioxide Reforming of Methane to Hydrogen and Syngas

Jie Deng, [a, b] Wei Chu,[*a] Bo Wang, [b] Zhenxin Xu, [a] Wen Yang, [a] Xiu Song Zhao[*b]

1.Catalyst Synthesis

Preparation of the ordered mesoporous ceria (*m*CeO_2): the well-ordered mesoporous nanocrystalline ceria were prepared using an improved evaporation induced self-assembly strategy (EISA) through the delicate control over the volatile process, followed by encircling EN species and thermal treatment. This EISA strategy has been well developed and widely applied to synthesize a variety of the ordered mesoporous oxides, such as Al_2O_3, TiO_2, $CeZrO_2$, ZrO_2, Nb_2O_5, and CeO_2,.[1] Typically, 1 g triblock copolymer $HO(CH_2CH_2O)_{20}(CH_2CH(CH_3)O)_{70}(CH_2CH_2O)_{20}$ (Pluronic P123, M_n=5800, Sigma-Aldrich) was dissolved in 20.0 mL absolute ethanol, stirred for 0.5 h at 25 °C, and then sonicated (40 kHz, 250 W cm^{-2}) for 15 min. A transparent solution was derived. Afterwards, 10 mmol $CeCl_3.7H_2O$ was added. After magnetically stirring for no less than 5 h at 25 °C, the resulting homogeneous sol solution was transferred to an oven and gelled under the pre-set conditions (temperature: 40 °C, relative humility: 50%) until a golden yellow xerogel glittering with the metallic luster was derived. In this procedure, the inorganic precursor hydrolyses and polymerizes into a metal oxide network. The gel product was first dried at 100 °C for one day, and subsequently thermally treated at 200 °C for 5 h to stabilize the network. Then, the as-prepared powders were exposed to the reflux in the ethylenediamine (EN) aqueous solution for 2 days at approximately 90 °C in the pH value of roughly 11. Afterwards, the products were washed by distilled water several times and dried at 100 °C for 24 h. Finally, the resulting powders were first calcinated at 350 °C in N_2 atmosphere for 4 h to stabilize the mesostructure framework and then thermally treated at 600, 700, 800, and 900 °C at ambient atmosphere for 4 h to eliminate the organic template and enhance the crystallinity.

Preparation of the rod-like ceria (*r*CeO_2): a hydrothermal strategy was employed to obtain the ceria nanorods as previously described. [2] Briefly, 1.74 g of $Ce(NO_3)_3.6H_2O$ and 19.2 g of NaOH were dissolved in 40 ml of distilled water under magnetic stirring for 0.5 h, respectively. Subsequently, these two solutions are mixed together and kept magnetic stirring for 0.5 h. The resulting mixture was afterwards transferred to a 100 mL Teflon-lined stainless steel autoclaves, and maintained at 100 °C for 1 day. After naturally cooling the autoclave to 25 °C, the resulting slurry was collected by centrifugation, washed with distilled water and ethanol several times, dried in vacuum at 80 °C overnight, followed by the N_2-activation mode at 600 °C for 4 h to ensure the sufficient surface defects and

the stable size and shape during subsequent loading of Ni nanoparticles and reaction tests.[2]

Preparation of nickel nanoparticles supported on *m*CeO_2 (NiCe-Cav) and *r*CeO_2 (NiCe-Vex): the nickel nanoparticles were generated in the internal concavities of *m*CeO_2 or on the external concavities of *r*CeO_2 by the modified incipient wet impregnation approach using the as-prepared ceria nanomaterials as supports. Generally, the desired amount of $Ni(NO_3)_2.6H_2O$ were dissolved in 5 mL of distilled water, and afterwards 0.5 g of ceria nanomaterials were impregnated in the solution under stirring. After impregnation under sonication conditions for 1 h, the impregnates was exposed to drying under the dynamic vacuums first at 25 ^oC for 1 day to evaporate water and then at 120 ^oC overnight to further effectively remove water. The resulting samples was activated by the plasma treatment as detailed previously.[3] The effective water removal at low temperature via the vacuum-drying can prevent the premature hydrolysis, thereby avoiding the large metal agglomerates and bimodal size distributions as previously reported.[4] The use of plasma has been proven efficient for preparation of heterogeneous catalysts due to the unusual chemical reactivity that can be achieved in a plasma environment.[5] The Ni loading on ceria supports is 7 wt. %, as determined by ICP-AES.

Preparation of NiO nanoparticles: NiO nanoparticles were prepared by a homogeneous precipitation method. Typically, $NiCl_2 \cdot 6H_2O$, sodium dodecyl sulfate, urea, and de-ionized water with a molar ratio of 1:2:30:60 were mixed, stirred at 313 K to yield a transparent solution and then kept at 353 K for 20 h. The water insoluble product was then filtered and washed with de-ionized water until no presence of chloride species followed by rinsing with ethanol for several times. The resultant solid was dried at 353 K for 12 h and calcined at 573 K for 4 h to produce brown powders.

2. Characterization

All treated samples including samples reacted and reduced were cooled down to 25 ^oC under the N_2 flow (30 mL/min) and sealed as described in the literatures[7] prior to characterizations.

X-ray diffraction patterns (XRD) were obtained with the X-ray diffraction apparatus (Philips X'pert PRO) using Cu Ka (45 kV, 50 mA) radiation.

N_2 adsorption-desorption isotherms at -196 ^oC were measured on tristar II 3020. Initially, all samples were degassed at 200 ^oC overnight before tests. The specific surface areas were computed employing the Brunauer-Emmett-Teller (BET) equations.

Transmission electron microscopy were operated on Tecnai G2F20 transmission electron microscopy. The samples were dispersed in ethanol assisted by the ultrasonic technique, and then deposited on a TEM grids.

CO-temperature programmed desorption (CO-TPD) was done in a fixed bed reactor. Before experiments, the samples were pre-treated at 550 °C in H_2 for 1 h, and then purged in an argon flow at 550 °C for 1 h. Afterwards, the samples were cooled down to 50 °C in the flowing argon, and exposed to the CO flow (30 mL/min) for 1 h for adsorption. Then, the samples were exposed to purging using an argon flow at 50 °C for 2.5 h to remove the physically adsorbed CO molecules. Finally, the temperature was raised linearly to 800 °C at a heating rate of 10 °C/min. The effluents were continuously monitored by the on-line quadrupole mass spectrometer. Immediately after the CO-TPD, the samples were again cooled down to 25 °C in an argon flow, and the temperature-programmed oxidation was performed. In this case, a 10% O_2/Ar mixed gases (50 mL/min) were introduced and meanwhile the system was heated linearly to 800 °C at a rate of 10 °C/min. The emission of CO_2 was recorded by the on-line quadrupole mass spectrometer.

Chemisorption of H_2 was conducted in an auto chemisorption analyzer. The samples were first dried in helium at 250 °C for 2 h and reduced in situ by H_2 at 550 °C for 1 h at a ramp of 10 °C/min. The catalysts were flushed by helium at the reduction temperature for 2 h, and afterwards cooled down to 30 °C in vacuum to implement the chemisorption tests.

X-ray photoelectron spectra (XPS) were registered on an XSAM800 spectrometer with an Al Ka (hv=1486.6eV) X-ray source, and the binding energies were corrected using C (1 s) at 284.6 eV to eliminate charging effect.

Element contents were obtained via inductively coupling plasma atomic emission spectrometry (ICP-AES).

H_2-temperature programmed reduction (H_2-TPR) was performed with a fixed-bed reactor. Samples were subjected to a 4.2% H_2/N_2 mixed gas (30 mL/min) from 100 to 800 °C at a heating rate of 5 °C/min. The H_2 evolution was detected online by a SC-200 gas chromatograph with a thermal conductivity detector (TCD).

Raman spectra of catalysts were recorded using an excitation wavelength of 514 nm (visible) or 325 nm (UV) on a Renishaw (RM2000) spectrometer.

The pulse experiments were conducted at 550 °C. The temperature of 550 °C rather than 700 °C or higher (at which the total reactant conversion is achieved) is based on a compromise between the catalytic activity and the energy input consumption. Because at 550 °C a satisfactory behavior with conversion above 50 % under the steady-state condition is gained, this temperature is prioritized for the pulse study to derive insights into exploring the nanocatalysts with the excellent reactivity at low temperatures. The interaction of CH_4, CO, and CO_2 with the Ni-CeO_2 catalysts was studied employing pulse reaction tools. The transient pulsing was carried out in a gas-phase quartz micro-reactor (i.d.=4 mm, length=50 mm). Typically, the catalytic materials in a fine powder form

(sieve fraction of 250-500 μm) were charged in the middle of the quartz reactor, and the other spaces of the reactor was filled with the 250-450 μm quartz sand in order to shorten the residence time of reactants and products for quickening the transient response speeds of the pulse signals. The height of catalyst beds is about 2 mm. The temperature was measured by a thermo-couple positioned in the center of the catalyst bed, and the reactants and products were recorded at the reactor outlet by an on-line quadrupole mass spectrometer. Prior to the experiment, samples were pre-reduced in situ at 550 ^{o}C for 1 h in a H_2/N_2 = 1:9 flow, and then purged in a flowing He for 1 h. In the course of the pulse tests, pulse gases of CH_4/Ar =1/1, or CO_2/Ar = 1/1 were injected into the helium carrier gas flow (45 mL/min), and then continuously passed through the reactor. The interval between consecutive pulses was roughly 4 minutes. Pulsing of a different gas was introduced after stabilization for 0.5 h under the continuous helium stream. The argon here served as an internal standard for data evaluation.

In situ X-ray diffraction measurements were carried out on the a Bruker D8 Advance Diffractometer employing the monochromatic Cu Kα1 radiation (40 kV, 40 mA, λ=1.54056 Å). Initially, powdered catalysts were subjected to reductive treatment under H_2 at 550 ^{o}C for 1 h, and afterwards cooled down to room temperature in inert atmosphere. The reduced catalysts were charged into the X-ray reactor chamber, purged with the helium flow for 0.5 h, and finally heated to 550 ^{o}C in helium flow. Then, the CO_2 or the CO_2/CH_4 (1:1) were introduced. A 2θ survey scan was implemented between 38^{o} and 46^{o}, and the spectra were recorded every 5 min.

Thermogravimetric analysis (TGA) was performed on a Q500 thermogravimetric analyzer. The catalysts were heated in a flowing air from 25 ^{o}C to 800 ^{o}C at a ramp of 10 ^{o}C/min.

Room-temperature Fourier transform infrared (FT-IR) spectra were recorded on a Bruker Tensor 27 Fourier transform spectrometer.

Prior to the temperature programmed desorption of carbon dioxide (CO_2-TPD), 50 mg samples were reduced in situ by H_2 at 550 ^{o}C for 1 h, and purged at this temperature for 2.5 h in helium flow. After cooling down to 50 ^{o}C, a CO_2 flow of 30 mL/min was passed over the samples for 1 h for adsorption. Finally, the gaseous and weakly adsorbed CO_2 molecules were eliminated through flushing with a steady helium flow for 2 h. The samples were then heated linearly to 800 ^{o}C at a ramp of 10 ^{o}C/min. The desorbed CO_2 was detected by TCD.

3.Supplementary data

3.1 Textural properties of mesoporous CeO_2 support nanomaterials

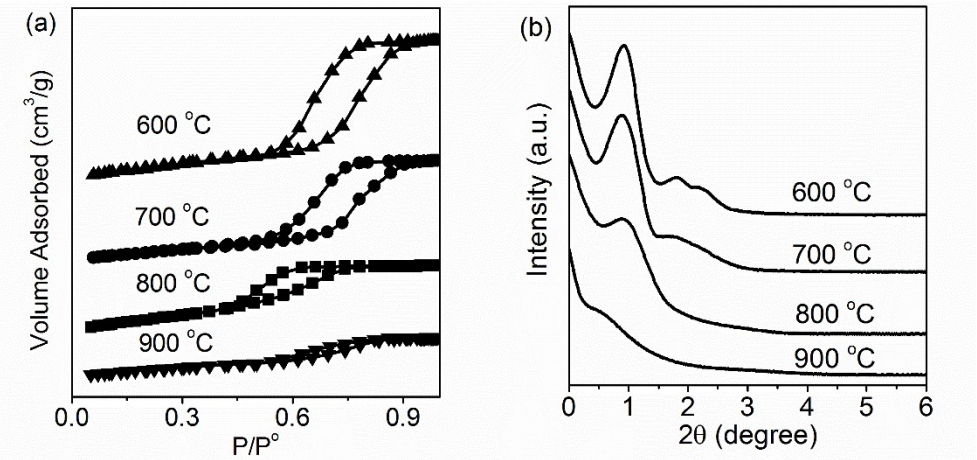

Fig.S1 N_2 volumetry (a) and low angle XRD patterns (b) of the as-prepared *m*CeO_2 calcinated at different temperatures.

All isotherms with the marked leap at the relative pressure of 0.5-0.85 in Fig.S1a are type IV, which refers to the mesoporosity to the as-prepared materials. The isotherm for *m*CeO_2 calcinated 600 °C presents the H1 hysteresis loop, indicating the presence of the cylindrical mesopores, which agrees well with the TEM and small angle XRD results. This hysteresis behavior is reported to be linked with the capillary condensation in the large pore channels with the possible channel modulation. The steepness of the capillary condensation steps indicates a high degree of mesopore uniformity. With the increase in the calcination temperature, the steepness of the capillary condensation steps becomes increasingly weak and the capillary condensation steps was shifted to the lower relative pressures, showing the decrease in the mesopore uniformity and size, respectively. This suggests the thermal treatment will cause the mesoporous structure to deteriorate, distort, deform, and/or shrink. When the sample was calcinated at high temperature, particularly above 800 °C, the small adsorption quantity and broad capillary condensation step hint at a substantial collapse of the ordered mesoporosity. As a result, the isotherm seriously deviates from the H1 type, and become increasingly akin to the hysteresis loop H2 or H3, implying that the pore structure collapse or contraction leads to the formation of some new types of pores or channels, for example, the cage like mesopores, the packed slits, and/or mesopores with constrictions.

Characteristic small angle XRD patterns of the mesoporous ceria (*m*CeO_2) materials thermally annealed at various temperatures are depicted in Fig.S1b. Generally, the small angle data can unveil that the thermal-annealing exerts a significant impact upon the generation of the mesoporous architecture. The *m*CeO_2 calcinated at 600 °C presented a sharp major peak at around 1 degree along with two well-resolved weak minor peaks nearby 1.8 degree and 2.5 degree, which can be indexed into the 100, 110, and 200 reflection planes, respectively. Such diffraction lines clearly show that the highly hexagonal ordered mesoporous structure (space group p6mm symmetry) was formed

within the framework of the CeO_2 materials. Noteworthy, the obvious (100) diffraction peak and the weak (110) peak were still detected on *m*CeO_2 calcinated at 700-800 °C, implying that the heat treatment did not significantly destroy the mesoporous structure. The peak intensity for the as-fabricated materials decays gradually with the increase in the calcination temperature, suggesting that the highly organized meso-structure might get distorted partially or destroyed to some extent. The ordered meso-porous network was preserved after calcination at 800 °C, showing a good thermal stability. However, it is observed that the XRD spectrum for *m*CeO_2 calcinated at 900 °C is almost featureless, with the 110 and 200 reflections vanishing and the 100 diffraction too weak to discern, indicating the lack of the obvious ordered mesoporosity and the substantial collapse of the meso-structure. In short, this illustrates that some mesopores are destroyed or collapsed when the calcination temperature exceeds 800 °C, while the well-organized mesopores are collapsed or destroyed seriously when the calcination temperature is up to 900 °C.

3.2 Crystal phase structure of the *m*CeO_2 support

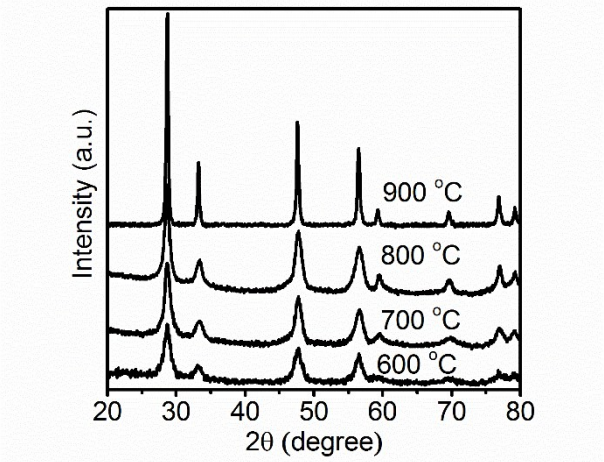

Fig.S2 Wide angle XRD patterns of *m*CeO_2 calcinated at various temperatures.

3.3 NiO Particle Size Distribution

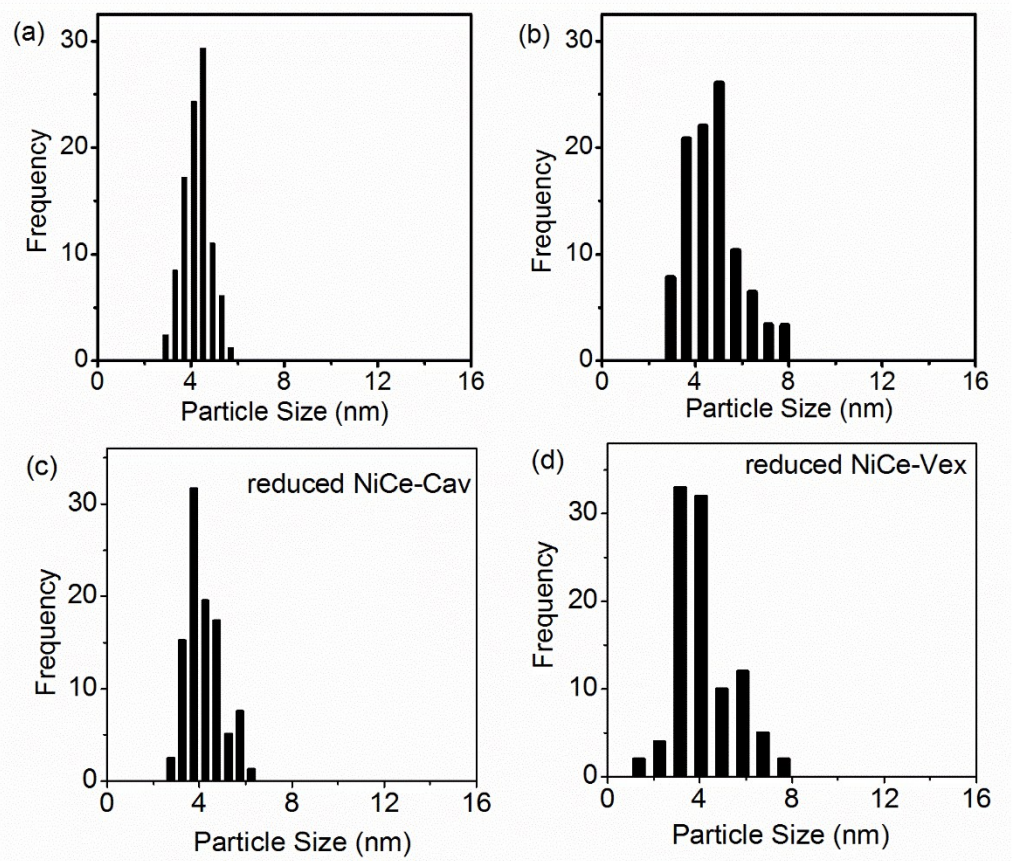

Fig. S3 NiO particle size distribution: (a) NiCe-Cav calcinated at 700 ° C; (a) NiCe-Vex calcinated at 700 ° C; (c-d) samples reduced at 650 °C.

3.4 Wide Angle X-ray Diffraction patterns of NiCe-Cav and NiCe-Vex

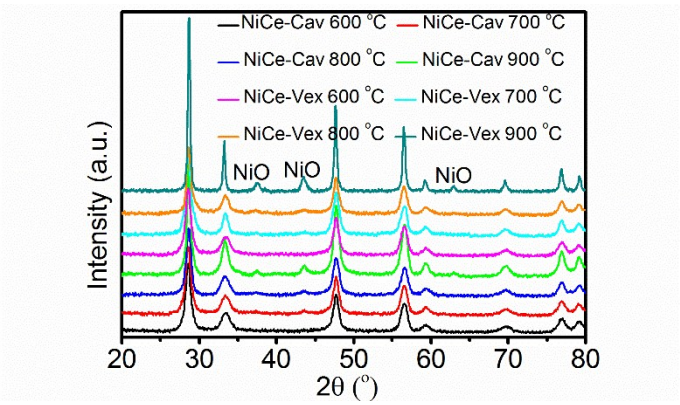

5

Fig.S4 XRD patterns of NiCe-Cav and NiCe-Vex thermally annealed at different temperatures.

3.5 Hydrogen temperature programmed reduction (H_2-TPR)

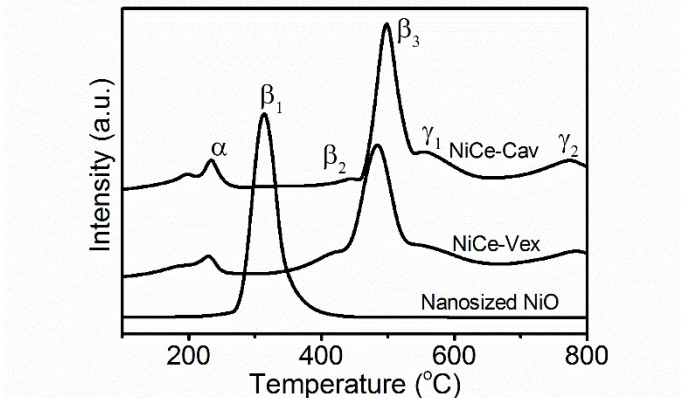

Fig. S5 TPR profiles of fresh NiCe-Cav, NiCe-Vex, and nanosized NiO NCs

As has evidenced in our previous work, there emerged two envelopes for the pure CeO_2, a very weak one at 655 °C and a big broad one ranging from 780 °C to 900 °C, which were relevant to the reduction of the outermost and innermost shell lattice oxygen of ceria, respectively.[6a] In Fig.S5, the nanosized NiO gave a single symmetric peak at 320 °C (β_1). However, the hydrogen consumption for the NiCe-Cav and NiCe-Vex was distinct from that for the pure NiO and CeO_2, and divided into the multiple well-characterized regions. The low temperature peaks below 240 °C (α) was assigned to the surface oxygen species adsorbed on surface oxygen vacancies, caused by generation of Ce-Ni addicts or formed during the synthetic process of supports. These adsorbed oxygen molecules were very reactive oxygen species and ready to be reduced by H_2 at low temperatures. Therefore, the intensity of the α region can be determined by the population of the oxygen vacancies on the oxide surfaces. The similar integrated area under the α peak clearly suggests that the superficial densities of oxygen vacancies on NiCe-Vex and NiCe-Cav are quite close. This is also an important indicator for the similar interaction between Ni and CeO_2 on both two samples.

The reductive process of NiO for both two samples significantly shifted to the high temperature of 485-500 °C (β_3), almost 180 °C higher than that of nanosized NiO. This was due to the complex NiO species which strongly interacted with CeO_2, most possibly the local Ni-O-Ce chemical bonds.[6b] The considerably higher reduction temperature than the pure nanosized NiO clearly showed that the Ni-O bond in NiCe-Cav and NiCe-Vex was stronger than that in the pure bulk NiO. This strong Ni-O bond in the Ni-Ce complex arises from the fact that when occupying or bonding with the Ce^{4+} sites around interfaces the Ni^{2+} was forced to possess a very large number of oxygen neighbours forming the stronger Ni↔O↔Ce exchange near boundaries than the Ni↔O↔Ni interaction in the rock salt structure. The maxima of peak temperature and the integrated peak area of β_3 on both two catalysts are analogous, clearly reflecting that interaction between Ni and CeO_2 for two samples is quite similar. The wide bumps at 540-550 °C (γ_1), as the shoulder peaks of β_3, hint that the reduction of NiO was simultaneously accompanied by the reduction of surface lattice O^{2-} anions. The maxima reduction temperature of γ_1 was very close on both samples but about 100 °C

lower than those of pure CeO_2, hinting the similar activation barrier for removing O species in the fluorite structures on NiCe-Cav and NiCe-Vex and the similarly promoting effect of the Ni loading on the CeO_2 reduction, respectively. Indeed, H_2-TPR data implies a robust and similar interaction between the Ni and the Ce species which substantially favoured the redox kinetics of both two samples.

3.6 X-ray photo electronic spectra

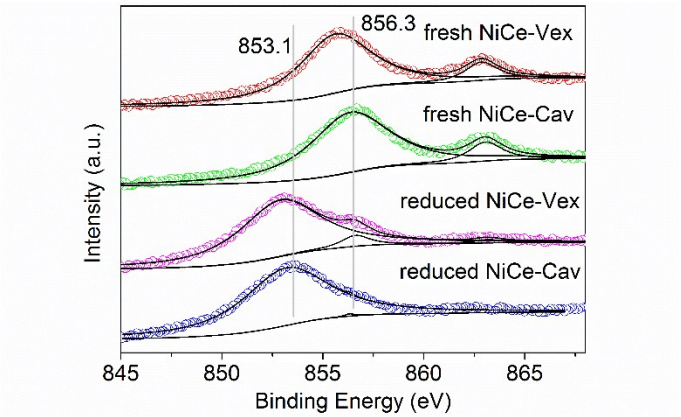

Fig. S6 Core level XPS spectra of Ni2p on all fresh catalysts and reduced catalysts

As shown, on the fresh samples, Ni can be found in ionic status because of the final preparation step. The peaks centred at about 856.2 eV along with the shoulder peaks at around 862.3 eV are assigned Ni^{2+} species. However, the measured binding energies for Ni^{2+} are dramatically higher than typical values for bulk NiO (854 eV).[7] When Ni intermixed or strongly interacted with metal oxides, Ni 2p binding energies above 856.0 eV are widely reported. [8] Thus, it is tempting to assign the detected Ni 2p signals to the NiO strongly interacting with the ceria supports. Reductive treatment using H_2 leaded to the full conversion of Ni to the metallic status. The measured binding 853.2 eV binding energies in NiCe-Cav and NiCe-Vex is to some extent larger than the bulk binding energy [9]. Overall, XPS results indicate the obvious electron transfer from the Ni to Ce. This electronic interplay may arise from the initial and final state effect caused by the low coordination of the Ni atoms in very small clusters [10]

3.7 Study on the mass transfer limitations

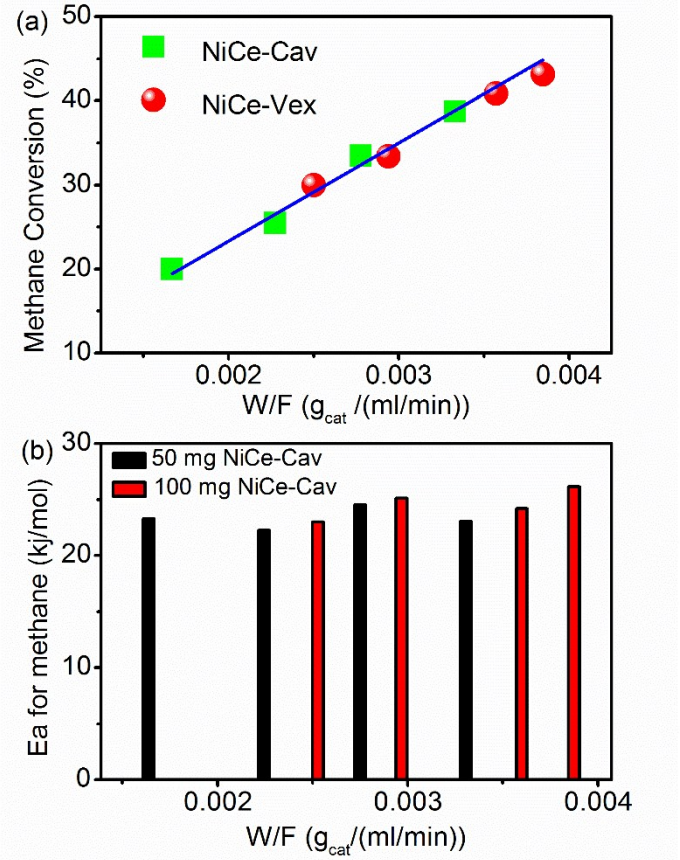

Fig. S7 (a) Methane conversion at 500 °C and (b) apparent activation energy for the CO_2-CH_4 reforming at various catalyst/feed ratios (W/F) over 50 mg and 100 mg NiCe-Cav;. Conditions: P=0.1 MPa, CH_4/CO_2=1/1

The potential mass transfer influence on the catalytic system was assessed by changing the flow rates of reaction gases. Two different weights of NiCe-Cav, 50 mg and 100 mg, were charged for examining the mass transfer limits. The W/F-CH_4 conversions at the low temperature of 500 °C are paradigmatically given in Fig.S7a. It is clearly seen that the WF-CH_4 conversions nearly follow the same line. In addition, the tested activation energy (Fig.S7b) was observed to be practically independent of the flowing rates (Ea=23.3±2.5 kJ/mol). These unambiguously suggest that the mass diffusion limit can be excluded in the investigated W/F ranges. Enormous studies about the CO_2/CH_4-reforming on the porous materials-supported metal nanocatalysts clearly evidence that under the typical CO_2-CH_4 reforming conditions the intrinsic reactivity can be negligibly impacted by the mesoporosity-induced mass transfer limit but be almost predominated by the intrinsic properties of catalysts, *e.g.*, chemical natures of supports (such as the acidity-base properties and redox), support-metal interaction, the morphostructure features of active component (such as particle size, geometrical shape), and/or the defect chemistry of each components.[11] If the increased inherent reactivity on NiCe-Cav in sharp contrast with those on NiCe-Vex for the CO_2-CH_4 reforming might be due to the possible mass transfer limit rather than an inherent nature of NiCe-Cav, kinetic data on active nickel

components entrapped inside in inactive mesostructured carriers such as, Al_2O_3, and SiO_2, should be much inferior to these simply deposited over the inert support particles. Actually, the measured intrinsic reactivity on Ni NPs embedded within the inert mesoporous materials are quite similar to these to that over Ni over their grains.[11] All in all, the mass transfer limit for our catalytic system on NiCe-Cav can be safely ruled out.

3.8 Turnover Frequency Values

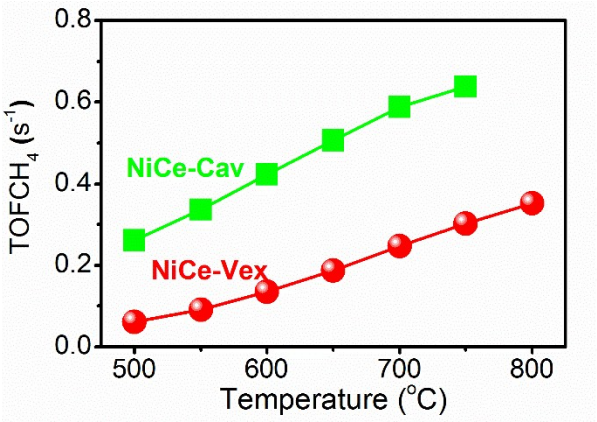

Fig.S8 Comparison of TOFs for the CH_4 conversion at different reaction temperatures.

3.9 Stablity Test

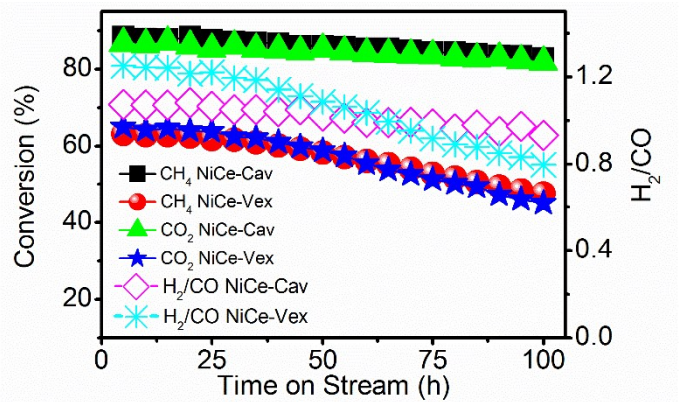

Fig.S9 The catalytic stability at 700 °C

3.10 Raman Spectra of used samples

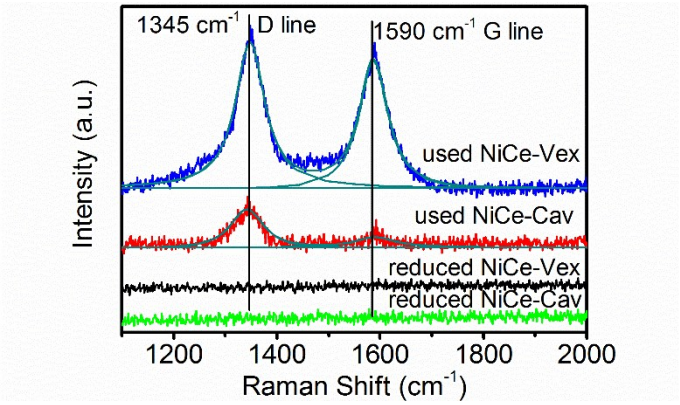

Fig. S10 Raman spectra of spent samples and reduced samples,

The role of the spatial positioning of Ni NCs in impacting the stability was further studied by Raman tools. In Raman spectra of spent samples, two peaks at about 1345 and 1590 cm^{-1}, well known as the D-line and G-line, respectively, are observable. G-line represents the breathing mode of carbon sp2 bonds of ordered graphite, whereas the D-line is sensitive to the stretching of sp3 carbon atoms with dangling bonds in disordered carbonaceous species.[13] The extent of the ordering of the carbonaceous materials can be roughly calculated quantitatively based on the integrated intensity of D and G liness. The greater microcrystalline planar size L_a defined as $4.4(I_G/I_D)$ implies the larger extent of ordering in carbonaceous materials.[14] As for the spent NiCe-Vex, the strong signals of D- and G- lines indicate a great deal of carbon deposits, in agreement with TG data. The L_a value on spent NiCe-Vex is 3.9 nm, considerably larger than that on spent NiCe-Cav (1.1 nm), suggests a much higher extent of ordering of carbon species. In sharp contrast, the tiny amounts of more disordered carbon, such as amorphous or defective filamentous, are formed on spent NiCe-Cav.

3.11 TGA analysis of spent samples

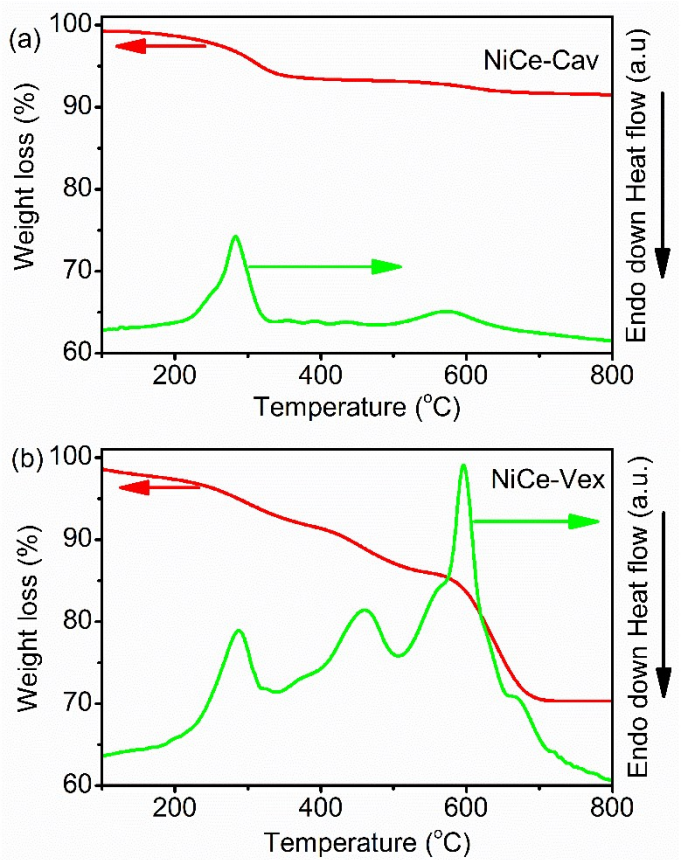

Fig.S11 TG/DTA profiles of spent NiCe-Cav (a) and NiCe-Vex (b)

The carbon deposits over the catalyst surfaces during the CO_2-CH_4 reforming can primarily contribute to the catalytic deterioration of catalysts, leading to the poor stability and reactivity. The most possible routes for generating cokes are as follows:

$2CO \rightarrow CO_2 + C$ (Boudouard or CO-disproportionation reaction) (R-1)

$CH_4 \rightarrow 2H_2 + C$ (CH_4-cracking) (R-2)

According to literatures[11], the primary pathway for coke formation over NiCe-Vex ought to arise from the catalytic CH_4 cracking. As well known, nickel phases are highly reactive for CH_4 decomposition particularly at high temperatures to lead to the CH_x fragments. When the CH_x species cannot be immediately oxidized by the oxidant immediates formed from the CO_2-activation, they would be very easily further oligomerized and transformed into a variety of inactive solid carbonaceous residues over the catalyst surfaces. In addition, the Boudouard reaction, a reversible exothermic reaction, has been evidenced as one key reaction route for carbon deposition. Li et al.[12] investigated the CO pulsing tests on the Ni-based catalysts and indicated that the Boudouard reaction could occur over Ni-based catalysts at about 600 °C. Therefore, a portion of cokes could also be formed through the Boudouard reaction in our catalytic measurement. Taken together, one can safely infer from the foregoing statements that the coking was induced via a combination of catalytic cracking and Boudouard reaction.

The coke formation over catalyst surfaces was probed with the TG-DTA technique under the oxidative atmosphere. The TG curves were employed to quantify the overall amounts of carbon residues on catalysts surfaces derived from the carbon elimination. It is needed to note that the weight loss peak around 100 ^{o}C is caused by the significant desorption of moisture, and that the weight loss arising from the coke residues was computed merely by the weight loss at above 110 ^{o}C to rule out the interference of moistures. It must be pointed out that a slight increase in weight caused by Ni^{o} oxidation could be included in the computations. Taking into consideration the identical Ni loading over both samples, the Ni^{o} oxidation was anticipated to equally contribute to the weight increase. The weight loss on CeNi-Vex pronouncedly outnumbered that on NiCe-Cav. The overall quantity of coke residues is only 7.75 % for CeNi-Cav but up to 28.23 % for NiCe-Vex, indicating that the spatial positioning of Ni active components by means of constructing the NP-in-concavities architecture played a very important role in oppressing the carbon deposition during the CO_2-CH_4 reforming reaction. The DTA profiles of the samples suggest that an exothermal phenomenon, *i.e.,* the oxidation of the deposited carbon, occurs. The multiple exothermic peaks appeared in the DTG profiles of the spent samples, and these peaks indicated the presence of different types of carbon species with different reactivities. It is generally considered that compared to reactive carbon, inert carbonaceous species require higher temperatures to be oxidized.[11] Thus, the exothermic peaks at low temperatures are attributed to active intermediate carbonaceous species, which are responsible for the formation of syngas. The peaks at high temperatures are assigned to the deposited carbon species hard to remove, which lead to the deactivation of the catalyst. In the case of the NiCe-Cav sample, there are two exothermic bands in DTA profiles, manifesting that two different kinds of cokes were formed during the stability measurement. The first one at the low temperature of 250-320 ^{o}C can represent the combustion of the amorphous carbons that are reactive species for generating syngas and hydrogen energy, while the other very weak ones emerging at high temperature of above 550 ^{o}C can be linked with the volatilization of the fibrous or filamentous carbonaceous species with the various extents of graphitization, which are inert and lead to the catalytic decay.[11] Significantly, the DTA profile for NiCe-Cav is predominated almost by the peak at 250-320 ^{o}C, suggesting that the carbonaceous residues over NiCe-Cav are primarily the reactive carbon species. These species are favourably generated in the course of the onset phase of the CO_2-CH_4 reforming reaction, principally by means of the gradual chem-dissociation of CH_4. In absence of oxygen species from the CO_2-activation or at the lower oxidation rate of CH_x species than their formation rate, such active carbons will gradually accumulate over catalyst surfaces and then easily convert partially into less-reactive carbons via the further dehydrogenation, polymerization, and rearrangement. The peak in the ranges of 320-500 ^{o}C for spent NiCe-Vex can be ascribed to oxidation of this carbon. Additionally, it could be seen that the intense and sharp exothermic peak cantered at approximately 600 ^{o}C for used NiCe-Vex governed its DTA profile. These phenomena implyed that the more carbonaceous species generated on NiCe-Cav were relatively reactive carbonaceous species, which can take part in the

reforming process as intermediates for producing the desired product and was advantageous to avoiding catalytic degrades to much great degree, while, on NiCe-Vex, more graphitic carbonaceous residues were produced. Formation of enormous graphitic carbonaceous deposits over the NiCe-Vex surfaces declined its performance in the durability experiments.

3.12 Carbon monoxide-temperature programmed desorption (CO-TPD)

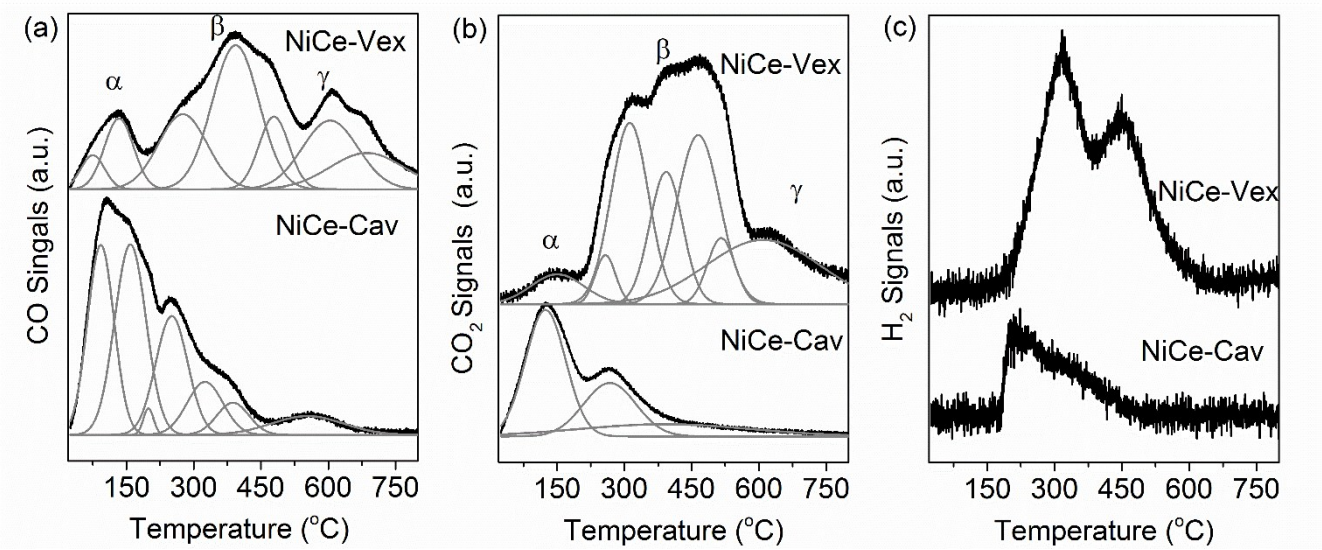

Fig. S12 Evolutions of CO (a), CO_2 (b), and H_2 (c) during CO-TPD on both samples**.**

The mechanism of desorption is a complex process and not always sufficiently comprehended. The rate of desorption is seen as a function of the coverage (θ) based on the following equation: $r=Kf(\theta)e^{-Ede/RT}$, where K is the rate constant, E_{de} is the desorption activation energy, and f(θ) is the fraction of the desorption centre at θ.[15] E_{de} has a relationship with the heat q and activation energy E_{ad} for adsorption ($E_{de} = E_{ad} + q$, q is a function of θ); and K can change due to both the variation of frequency of the superficial bond oscillation with θ and the superficial heterogeneity.[15] Because q decreases with the increase in θ, it can be well established that the rate of desorption is rapid at the low activation energy sites.

As observed in Fig. S12, CO desorption is accompanied by an appreciable generation of CO and an emission of small molecular hydrogen. CO_2 can be produced from part of CO through a combination of three possible chemical processes, *i.e.*, water gas shift reaction (WGS), the CO disproportionation reaction (Boudouard reaction), and direct oxidation by lattice oxygen (O_L) located metal-oxide interfaces or nearby the metals. WGS in the course of CO desorption takes place much possibly due to dehydroxilation of CeO_2 ($2CO+2OH_{ceria} \rightarrow 2CO_2+H_2$), while, with no abundant hydroxyl functionality over ceria surfaces, carbon monoxide undergoes disproportionation ($2CO \rightarrow CO_2+C$) or direct oxidation ($CO+O_L/e^- \rightarrow CO_2+\square_L/e^-$; $\square_L$: a lattice O vacancy sites). The elevated temperatures necessary for the desorption process can make the adsorbed layers highly loose and then get significantly mobile; consequently the equilibrium distribution of

adsorbates could interplay with one another, with hydroxyl functionality existent over the ceria support surfaces, or with O_L species stored inside ceria.

As seen from curves in Fig. S12a, all samples display three well-characterized peaks (α, β, γ) during a wide temperature range. The peaks at low temperature stand for desorption of low activation energy (E_{de}) centres, which leads to a small q and poor CO binding over the sample surface, with a corresponding high θ. The two chemisorption sites are believed to exist at the low θ, whereas the single-site chemisorption prevails at higher θ.[15a,16] According to literatures[15], the mixed one and dual centre chemisorption have been observed over Ni; and the nature of carriers plays a paramount part in deciding the kinds of adsorption and the quantity of desorption centres due to both the heterogeneity and the adsorption taking place over various lattice spacings. Fig. S12a demonstrates a single-site chemisorption at a high θ and low temperature range (0-200 ^oC), a multisite chemisorption mechanism dominating between 300 and 500 °C at the cost of low θ, resulting in a high heat of adsorption and high CO adsorption capacity, and a desorption of CO (>500 ^oC) as a result of re-combination of atomic carbons (C_s), which is formed by Boudouard reaction at relatively low temperature, with superficial O_L in support ($C_s+O_L/e^-\rightarrow CO+\square_L/e^-$)[17]. In short, the desorption peaks in Fig.S12 possess the various chemisorption heats in the sequence $\alpha < \beta < \gamma$ due to the inverse sequence of their θ. Significantly, the increment in the α peak intensity and the concurrent decline in the β and γ peak strength over NiCe-Cav relative to the NiCe-Vex catalyst, and the similar evolution trend of CO_2 emission can be likewise observed. The NiCe-Cav displays the most sharp and intense CO-desorption rate within the α zones when compared to the β and γ zones, indicating the substantial rise in the low heat adsorption centers. These data evidence that in sharp contrast with the Ni deposited the open external surfaces of ceria, the configuration of Ni NCs encapsulated inside the concave internal surfaces of the ordered mesoporous ceria might induce the apparent surface heterogeneity and various lattice spacing, thereby resulting in the remarkable drop of the dual-center chemisorption.

In addition, it must be stressed that the single-site chemisorption of CO over Ni surfaces corresponds to the linearly bonding configuration of CO over the step and facet edges, while the dual-site chemisorption to the bridged bonding geometry of CO over the Ni corner atoms, step and facet edges.[18] Even though the absolute reassurance of such issues could be not safe in the absence of the further investigation employing some state-of-the art in situ tools, e.g., FTIR, we can qualitatively and semiquantitatively infer from the CO-TPD data that the nanocrystals-in-concavities architecture preferentially decorates the undercoordinated nickel sites, *e.g.*, steps, edges, and corners.

3.13 Oxygen temperature programmed oxidation (TPO) after CO-TPD

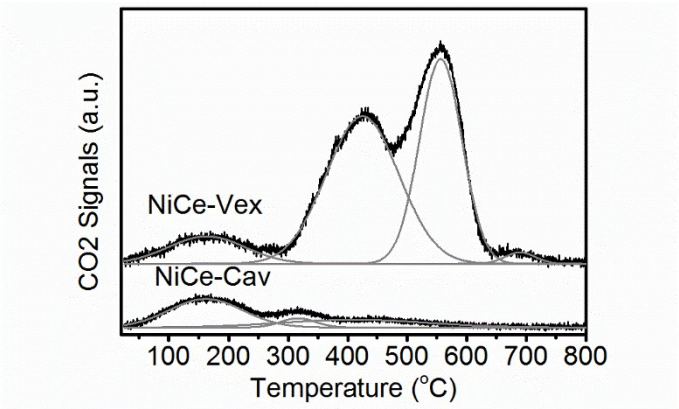

Fig.S13 TPO profiles of all catalysts after CO-TPD experiments

The extent to which Boudouard reaction occurred during CO-TPD experiments was probed by TPO; if the Boudouard reaction occurred, the combustion of carbonaceous, accompanied by the CO_2 emission, would be observed. The burning-off temperatures manifest the stability of the superficial carbonaceous species; and the larger temperature implies the poorer reactivity. Based on the preceding studies[19], gasification of carbon species usually occurred in three temperature ranges: <250 ^oC (atomic carbon), 250-500 ^oC (amorphous carbon), and >550 ^oC (graphic carbon). Although three peak zones are observed on both samples, but their relative distribution and intensity are distinct. In the case of NiCe-Cav after CO-TPD, the absolutely predominant peak between 100 and 300 ^oC is assigned to the highly reactive carbon or reaction immediates generated on the metal sites [20], which can react with oxygen at low temperature, while the weak peak between 200 and 400 ^oC is associated with amorphous carbon or Ni_3C generated around the metal-carrier interphase boundaries [21]. Noticeably, the peak corresponding to the graphic carbon was poorly resolved. In sharp contrast, NiCe-Vex after CO-TPD released substantially more CO_2, and the intense and sharp peaks above 300 ^oC assigned to the more stable and ordered graphic-like carbon predominated the whole profile. In general, the CO-TPD and TOP results markedly evidenced the crucial roles of the nano-scaled positioning shown here in mediating the interaction between the CO and the catalyst surfaces and its resultantly secondary transformation. This lowered CO binding energy and the consequently declined adsorption heats are the ideal properties for a reforming and/or conversion nanocatalyst since these traits can prevent CO from robustly favorably binding on the active phase surfaces while clearing up and freeing up that extra proportions of reactive centers accessible for targeted reactions.

3.14 Characterization after CH_4 pulse

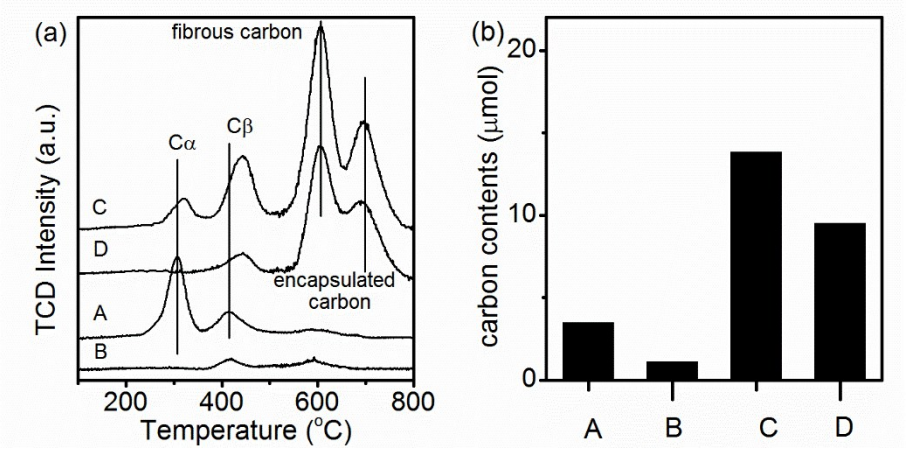

Fig. S14 (a) TPO profiles after CH_4 multipulse and (b) the corresponding contents of the carbon deposits formed during the CH_4-multipulse. A: the CH_4-multipulsed NiCe-Cav; B: the CH_4-multipulsed NiCe-Cav exposed to the CO_2 treatment; C: the CH_4-multipulsed NiCe-Vex; D: the CH_4-multipulsed NiCe-Vex exposed to the CO_2 treatment.

As discussed in the main paper, carbon deposits occurred during the CH_4 pulse. Because the TPO is the very sensitive technique for exploring reactivity of the carbonaceous residues and enables the quantitative and qualitative evaluation of their chemical nature, the samples after CH_4 pulse were in detail analysed using TPO to gain deeper insight into this phenomenon, and the results are shown in Fig.S14. Part of the CH_4-pulsed samples were subjected to the in situ oxidation by CO_2 at the temperature at which the CH_4 pulse was operated. To exclude the interference in the TPO signals of the decomposition or desorption of the possible CO_2-containing species (such as carbonates) formed during the CO_2 oxidation, the CO_2-treated samples were first exposed to purging in the Ar flow at 750 ^oC until no CO_2 signals were detected; certainly, for control, the non-CO_2-treated samples were also submitted to the same procedure to eliminate the potential impact of the Ar-purging on the surface carbon species formed from the CH_4-pulse.

As shown in Fig. S14, the CO_2 resulting from the oxidation of carbonaceous species by O_2 was the only carbon-containing product generated during TPO. For the NiCe-Cav and NiCe-Vex after the multi-CH_4 pulse, the various CO_2 signals were discerned within the certain temperature ranges. The NiCe-Cav and NiCe-Vex after the multi-CH_4 pulse were both characterized by two noted peaks at the low-temperature zones, one between 250 and 360 ^oC, the other ranging from 360 to 530 ^oC, while the other two strong and broad high-temperature peaks were practically visible only on NiCe-Vex. Though the CH_4-pulsed NiCe-Cav and NiCe-Vex both presented the low temperature peaks, some disparities were found concerning the oxidizing regions and their quantities. The CO_2 emission began at 250 ^oC for both samples, reached its first maximum at 305 ^oC for NiCe-

Cav and at 345 °C for NiCe-Vex, experienced its second zenith at 406 °C for NiCe-Cav and 450 °C for NiCe-Vex, and commenced up to 800 °C through the two well-identified maxima at 605 °C and 690 °C for NiCe-Vex. As stated in the main paper, the activation of CH_4 on Ni started with the generation of CH_x intermediates that can further completely dehydrogenate into the monoatomic carbon (C_α) species.[11] The first band between 250 and 360 °C represented such C_α intermediates. Nonetheless, lacking in oxidants or at the lower oxidizing rates, such C_α species will be readily converted into layers of the polymeric amorphous carbonaceous coatings, denoted as C_β,[11] which was more thermally stable and catalytically poorer in comparison with C_α, and, thus, was viewed to be gasified in the 360-530 °C ranges. Apparently, when compared to the CH_4-pulsed NiCe-Vex, the relative proportion of C_α to C_β were significantly higher and the C_α practically predominated the CO_2 release curve of the CH_4-pulsed NiCe-Cav. This discovery many lead one to reasonably conclude that this NC in concavities structure can have a very positive effect on oppressing the conversion of C_α to C_β. More importantly, after treating the samples with CO_2, the C_α species utterly disappeared but the C_β species were removed merely to some extent, indicating that the C_α species were more reactive towards CO_2 and that the C_β species were hard to remove once they were formed. The similar inference has been reported that the C_α species can be facilely volatilized by oxidant species such as CO_2 or lattice oxygen stored in supports to produce CO in reaction condition. Thus, these C_α species played an important role as reactive intermediates in the catalytic performance improvement.

Due to the great difficulty in oxidizing the C_β carbon deposits and its easy generation even at room temperature[18a], C_β species were highly prone to dissolve in nickel nanocrystallites to generate the transient metastable nickel carbide (Ni_3C), afterwards diffuse through and/or around the nickel granules to the metal/carrier interfaces, then precipitate, nucleate, conquer the interfacial interplays to form the vermicular carbon (C_γ), and eventually build up to grow into the fibrous carbon residuals (such as filamentous, tube-like, or whisker-shaped carbon).[11,19,21] The formation of this type of carbon can lead to detaching or hoisting the metal nickel nanoclusters from the carriers and capping the metal particulates. The stationary growing of fibrous carbonaceous deposits can be maintained via the continuous migration of C_β through nickel crystallites actuated by the carbon density gradient. This population gradient as a driving force for the bulk diffusion of carbon through nickel crystallites was caused by difference in the carbon level distribution between carbon-rich anterior nickel surfaces and carbon-deficient atomic nickel layers having a gradually decreased carbon concentrations to the bulk level of dissolved carbons. When the fibrous coke kept on growing, the nickel grains located at their apex stayed still reactive for the CH_4-decomposition but inert towards the carbon species oxidation by oxidants supplied by supports; meanwhile, if these carbonaceous deposits were enormously amassed, the reactor plugging and pressure accumulation throughout the whole reactor will occur. The strong and wide CO_2 signal between 530 and 650 °C, existent on NiCe-Vex but absent on NiCe-Cav, most presumably originated from the volatilization of some amounts of the fibrous carbons. This oxidation process

for the fibrous carbons has been considered as a reverse pathway of their formation, during which carbon first diffused back to the nickel surfaces for oxidation by O_2; and such carbon diffusion back to nickel surfaces has been suggested as the rate-controlling step for this fibrous carbon oxidation.[22] The signals for fibrous carbon oxidation unambiguously signified that a certain amount of reactive nickel centers favorable for the fibrous carbon formation exists on NiCe-Vex. In fact, the kinds of the active nickel centers for initiating the fibrous carbon and the reforming reaction are quite different. It is reported that the step edges on a large nickel nanodomain made up of 6 or 7 atoms is necessitated to produce superficial active carbonaceous transient precursors for further forming various sorts of coke, whereas a small nickel nanoentity merely including 3 or 4 atoms is needed for reforming reactivity.[23] Therefore, this disparity in the fibrous carbons on both samples reflected that high fractions of large nickel nanoensembles as active centers for carbon formation existed on nickel nanoparticles of NiCe-Vex.

This inference can be well understood in terms of the catalyst architectures. As analyzed in the main paper, the NiCe-Cav actually presented the nanoparticles-in-concavities configuration. Similar to tremendously studied encapsulating or embedding structures, such textural geometry leaded to an optimally engineered nanointerface, in which the nanocrystalline ceria walls both tightly surrounded the nickel nanoclusters giving a maximized nickel-ceria boundary, and exerted strain upon the closely contacted nickel nanoclusters distorting the perfect nickel crystalline structure. Therefore, around this engineered nanointerface, the microstructural arrangement of components, an abundance of edge sites, corner surface sites, defective sites, undercoordinated ions, and facile electron/oxygen transfer can occur, thereby both selectively blocking and preferentially stabilizing the coordinately unsaturated nickels sites such as steps and edges, which favored the full hydrogen stripping to generate C_α, through the strong interfacial adhesive force, and, meanwhile, breaking up the periodicity of nickel surfaces located around maximal metal/carrier interphase through dividing the nickel nanoparticles' into nanoensembles of nickel atoms that are too small to support coke generation. [24] In addition, the rapid Ni-NiO transformation (in Fig. 8) can in situ form NiO_x intermediates over the whole nickel nanoparticle surface, which partially decorated the nickel granules, and, thus, precluded or restricted the carbon dissolution. Even through this dissolution of carbon in the nickel crystallites took place via generation of a transient metastable nickel carbide species, the excellent oxygen mobility through interfaces can immediately hinder the carbon dissolution through oxidizing the instable nickel carbides. This explanation can be well in agreement with the standpoints in literatures wherein the roles of the metal-support nanointerface in inhibiting the carbon deposition and promoting the oxidation reaction were repeatedly emphasized and explored.

In addition, as shown in Fig.S14, the CO_2 treatment cannot oxidize the fibrous carbon, suggesting that the fibrous carbon were more thermally stable than the C_α and C_β, and quite inactive toward to CO_2.

Actually, not all C_β dissolved in nickel nanocrystallites and transformed into C_γ or fibrous carbon, while a portion of surface carbon atoms can reside over the gas side of

the nickel granules, then accumulate, and further encapsulate nickel granules, producing the graphitic carbonaceous coatings which can render the nickel active sites utterly inaccessible for reactants. In comparison with the C_γ or fibrous carbon, this capsulating graphitic carbon was more ordered and thermally stable, so a much higher oxidizing temperature was required. According to literatures, the detected band ranging between 650 and 750 ^oC over NiCe-Vex can be associated with such encapsulating carbon. Because the carbonaceous intermediates from CH_4-dissociation were produced on the whole surfaces of the nickel granules, particularly preferentially on the front nickel particles, they must migrate to the nickel/ceria interface areas for the oxidization reaction with oxidant species from carrier to yield gaseous CO. Apart from the spillovered oxygen species, an geometric factor can also contribute a lot to this formation of graphitic carbon on NiCe-Vex. In light of geometric standpoints, the carbonaceous species produced on surfaces of the nickel clusters with a quite smaller metal/support boundaries, especially when located at the front of nickel particles, must undergo a longer diffusion distance and path to the nickel/ceria interfacial perimeters in sharp contrast with carbonaceous species generated on nickel particulates with a maximized metal/support interface, as illustrated in Scheme 2 in the main paper. As a result, carbonaceous species on the nickel particles possessing the limited metal/support boundaries have longer time to react with each other, thereby facilitating the coke condensation or accumulation by yielding the greatly crystalline and ordered graphitic carbonaceous residuals. Such explanation, actually, can be cogently favored by TPO outcomes that maxima of the CO_2-release from combustion of the C_α and C_β species over NiCe-Vex displaced towards more elevated temperatures, namely, with the decreased metal/support boundaries. Furthermore, this encapsulation carbon cannot react with CO_2 as shown in curve c in Fig. S14a. These affluent carbonaceous residuals would trigger off complicated disturbance and alter the confinement environment in catalyst beds for the CH_4-pusling.

Fig. S14b gave the quantitative results (based on the peak area under profiles), the overall quantities of carbon deposited during CH_4 pulse is about 3.5 μmol for the CH_4-pulsed NiCe-Cav and 13.9 μmol for the CH_4-pulsed NiCe-Vex, of which up to 68 % for the CH_4-pulsed NiCe-Cav but only 30 % for the CH_4-pulsed NiCe-Vex can be reactively removed by CO_2. The total amounts of carbon deposits determined by the TPO tools was very close to the values calculated from the carbon balance.

During the CH_4 pulse, in order for the catalysts to form the smallest carbonaceous residuals, the oxidation reaction process most possibly took place prior to the full dehydrogenation of CH_x fragments into the monoatomic carbon species and/or the polymeric amorphous carbonaceous coatings. Taking into consideration both the larger CH_4 conversions yet a much lower total quantities of carbon deposited over NiCe-Cav than NiCe-Vex and the distinct coke formation trends in terms of their carbon types and amounts, this can safely result in the reliable postulation that the NC-in-concavities architecture exerted an important impact upon oppressing the full dehydrogenation of the CH_x fragments or/and its subsequent dissociation in nickel nanocrystals. Overall, CH_4-pulsing and TPO tests clearly displayed an appreciable discrepancy between NiCe-Cav

and NiCe-Vex that can account for the good tolerance of NiCe-Cav against catalyst deactivation during reactions.

3.15 FTIR spectra of catalysts after CO_2-pulsing

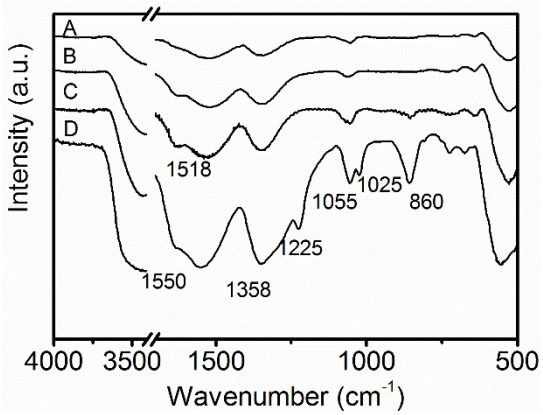

Fig. S15 FTIR spectra of the as-prepared NiCe-Cav (A) and NiCe-Vex (B), and the NiCe-Cav (C) and NiCe-Vex (D) after CO_2-pulsing experiment.

According to previous literatures, the spectra from 500 to 2000 cm^{-1} represent the characteristic vibrational modes of C-O/C-C. Within this regions, all samples displays the overall analogous features. The bands at about 1358 and 1518 cm^{-1} are assigned to the unidentate carbonates [25a], while the weak peaks at approximately 1225 cm^{-1} corresponds to the stretching mode of bridged carbonates [25b]. The peaks at about 1025, 1055, and 1550 cm^{-1} can be linked with the bidentate carbonates species. The peaks observed at roughly 860 cm^{-1} can be indexed into the π (CO_3) mode of carbonates [25c]. Ceria surfaces are well known to be sufficient in the oxygen vacancy defects. These defective sites are positively charged and thus possess high affinities with the negatively charged oxygen atoms in CO_2 molecules. Therefore, the carbonate species could be generated preferentially over the surface of ceria due to the reconstruction surface. These carbonates exist in the form of the cerium carbonates. The considerably stronger intensities of carbonates over NiCe-Vex after CO_2 pulse clearly show that plenty of thermal surface carbonates were formed while the rather limited quantity of carbonates are existent over NiCe-Cav after CO_2-pulse.

3.16 XPS spectra of catalysts after CO_2-pulsing

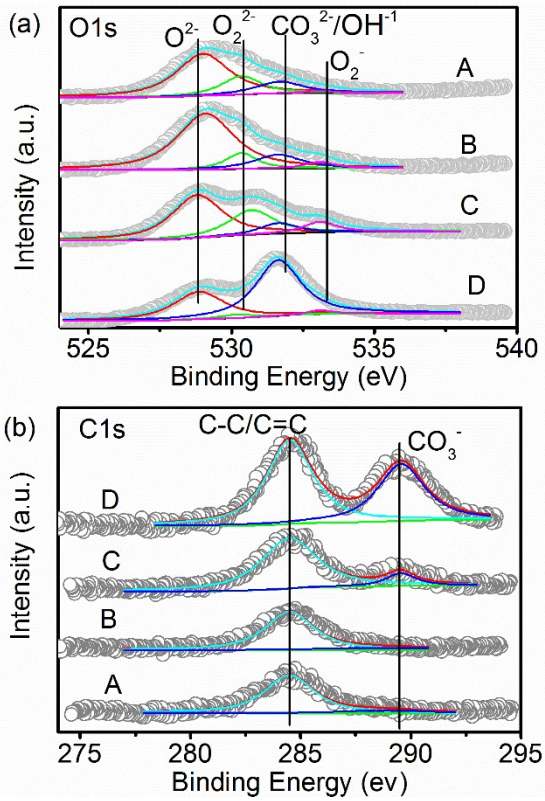

Fig. S16 O1s (a) and C1s regions (b) of X-ray photoelectron spectra. A: fresh NiCe-Cav; B: fresh NiCe-Vex; C: NiCe-Cav after CO_2-pulsing; D: NiCe-Vex after CO_2-pulsing

The O1s XPS of catalyst as shown in Fig.S16 (a) were employed to identify the coexisting oxygen species on the surface of the catalysts. The O1s spectra can be deconvoluted into four different peaks linked with the various oxygen species. They can be assigned to the oxygen ions in the crystal lattice oxygen O^{2-} (529.0), the peroxides O_2^{2-} (530.7 eV), the hydroxyls and carbonate species (OH^-/CO_3^{2-}) (531.6 eV), and the adsorbed O_2^- (533.1 eV).[26] These results indicate that the architecturally engineered Ni-ceria catalysts generate the oxygen vacancies in the ceria matrix due to particular synthetic strategies here. The O 1s BE value reported in this study consists with some prior reports. The fraction of each oxygen species varies much after CO_2-pulsing, indicating that the CO_2 adsorption/activation on the ceria surfaces during the CO_2-pulsing can appreciably modify the surface chemistry of ceria and that this decorating effects can vary much with the spatial positioning. When exposing to the CO_2-pulse, the ratios of surface electrophilic oxygen to lattice oxygen species, presented by $(O_2^{2-}+O_2^-)/O^{2-}$, in ceria surfaces, substantially declines on NiCe-Vex from 0.34 to 0.12 but significantly increase on NiCe-Cav from 0.25 to 0.29. In addition, the sharp and intense peak assigned to CO_3^{2-} is observed on the CO_2-pulsed NiCe-Vex. These data point to the fact that after CO_2 pulse the oxygen species are mainly existent in the atomic oxygen form on NiCe-Cav but almost in the form of CO_2-containing carbonates on NiCe-Vex. This phenomenon

clearly evidence the distinct activation mechanism of CO_2 on the various ceria surfaces. Some previous works have shown that these O_2^{2-} and O_2^- are thermally stable at high temperatures and conductive to the oxidation/activation of CH_4. Lunsford et al. reported that O_2^- can be durable at approximately 200 °C, and its reactivity increases with the temperature.[27a] Osada et al. demonstrated that O_2^- species were able to be stable up to 750 °C to react with CH_4 over Y_2O_3-CaO catalysts.[27b] Several studies have also experimentally and theoretically evidenced the role of surface peroxide O_2^{2-} ions as the active species for CH_4 activation. [27c, 27d]

The deconvolution of the C1s peaks show two kind types of carbon with different chemical states, which emerge at approximately 284.6 and 289.5 eV. The former can be ascribed to an elementary carbon (C-C/C=C) originating from the surface carbon contaminants or pump oil and/or from the hydrocarbon residues generated during the synthetic procedures. The latter can be linked with the carbon atoms bonded with several oxygen atoms (*e.g.,* carboxyl or carbonate groups), which results from the interaction of ceria surfaces with carbon dioxide. [28] As clearly seen, there are negligible carbonate species on both fresh samples, whereas after exposing to CO_2-pulsing, a great deal of surface carboxyl or carbonates exist on NiCe-Vex, suggesting that CO_2 can strongly bond with the convex surfaces of rod-like ceria to form the relatively thermally stable carbonate species.

3.17 Carbon dioxide-temperature programmed desorption (CO_2-TPD)

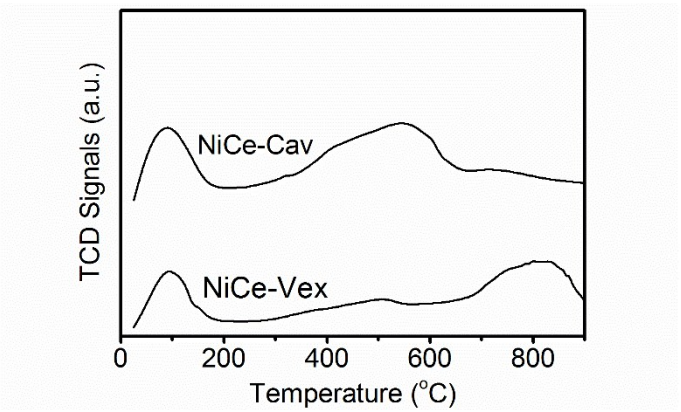

Fig. S17 CO_2-TPD profiles of the NiCe-Cav and NiCe-Vex.

The adsorption of CO_2 over the ceria or ceria-based materials is quite complex, and varies with the catalyst chemical composition, preparation method, and physiochemical properties.[29] The desorption behavior of CO_2 over ceria or ceria-based materials reflects its interaction with the catalyst surfaces. Generally, the stronger the interaction of CO_2 with the catalysts, the higher the desorption temperature of CO_2. As clearly seen from the profiles, there are three well-identified desorption regions occurring at 25-200 °C, 300-600 °C, and above 700 °C. Their distribution and strength on NiCe-Cav are distinct from those on NiCe-Vex, indicating the different kinds of the CO_2-adsobing sites. It is reported

that these reactive surface sites originate from the surface heterogeneity, namely, edges, corners kinks or/and structural defects such as some overlapping regions of crystal planes and that some small stepped trances expose or engender the coordinately unsaturated and positively charged centers which can interact with the negatively charged oxygen atoms in CO_2 molecule to form the "carbonate-like" species.[29] The first desorption peak corresponds to the reactive desorption of CO_2 interacting with weakly basic hydroxyl groups on ceria. The second one is assigned to the CO_2 adsorbates on the surface coordinately unsaturated O^{2-} anions. The peak above 700 ^oC can be linked with the structural carbonates resulting from the reaction of bulk lattice oxygen with CO_2.[29] According to the peak area and intensity, the dominant CO_2-adsoption sites occurs between 300-600 ^oC for NiCe-Cav but above 700 ^oC for NiCe-Vex. It must be pointed out that this temperature range for the dominant CO_2-desoption regions well coincides with the temperature needed for achieving a high CO_2 conversion of 60%-100%. From the viewpoint of the thermodynamics, the high desorption temperature means a strong binding at the high heat adsorption sites. Thus, from the CO_2-TPD, we can conclude that the CO_2-adsorption reactive sites are governed by the high heat adsorption centres on the convex *r*CeO_2 surfaces but by the low or medium heat adsorption centres on the concave *m*CeO_2 surfaces.

3.18 Stability of the active oxygen species on surface of cat1 by CO_2-pulse

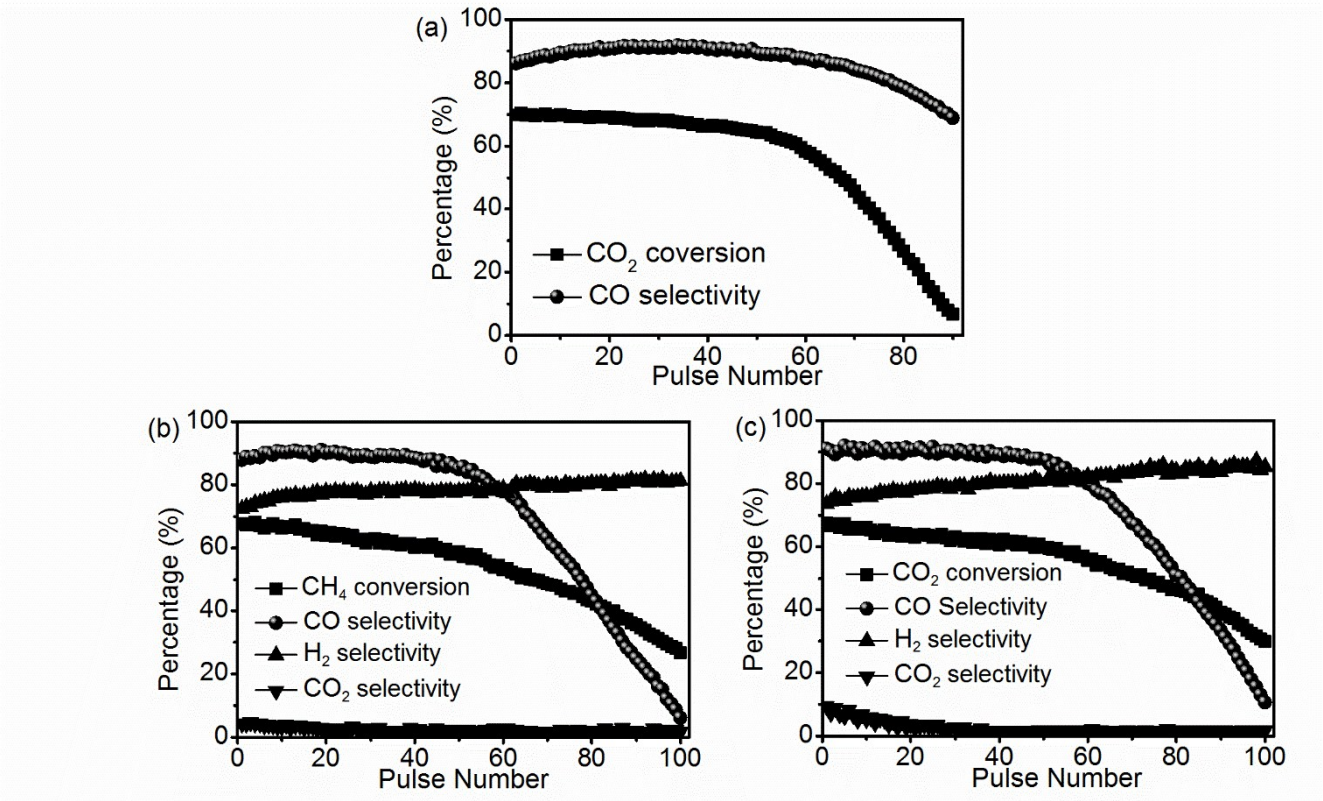

Fig. S18 Reactivity of CH_4-multipulses at 550 ^oC on the deeply reduced NiCe-Cav derived after CO_2-pulse pre-treatment with (b) or without (c) 5 h interval between CH_4-pulsing and CO_2-pulsing. Reactivity of CO_2-pulse is shown in a

Initially, NiCe-Cav was exposed to a deep reduction at 650 ^oC for 2 h for the removal of the available oxygen species stored in ceria, and then the temperature was cooled down to 550 ^oC for the pulse experiments. When pulsing CH_4 on the reduced NiCe-Cav, no oxygen-including products (CO, CO_2, or H_2O) were detected. This clearly shows that this deep reduction treatment can effectively eliminate the reactive oxygen species accessible for the oxidation of CH_x species at the reaction temperature of 550 ^oC. Fig. S18a displays the evolution of the CO_2 conversion and the CO selectivity over the reduced NiCe-Cav with the pulse number. The initial reactivity is comparable to that over the NiCe-Cav reduced at 550 ^oC, as shown Fig. S18a. It is found that, after about 90 pulses, the CO_2 conversion reaches below 5 %, suggesting that 90 CO_2-pulses are sufficient for re-oxidizing the reduced sample or supplanting the ceria oxygen vacancies created during the reduction treatment. The total amount of the oxygen species formed via the CO_2 dissociation or vacancy filling is computed to be roughly 104.2 μmol. When the subsequent CH_4-multipulsing was not conducted immediately after the CO_2-multipulsing, but with an interval of 5 h between the CO_2-pulsing and the subsequent CH_4-pulsing, simultaneously with the Ar-purging during this 5 h delay. Such treatment was employed to probe the thermo-durability of the oxygen species deposited from the CO_2-dissociation. Interestingly, excepting the traces of CO_2 that might arise from the desorption of the inappreciable amount of the surface carbonates formed during CO_2-pulsing, no MS signal for the gaseous O_2 was monitored, unambiguously indicating that the oxygen species deposited from the CO_2-dissociation were stable against the desorption as the molecularly adsorbed oxygen. More importantly, the subsequent CH_4-pulse, following by the time interval, gave an excellent initial reactivity with a CH_4-conversion of above 68 % and a CO-selectivity of above 90%. Considering the fact that no CO release during CH_4-pulsing was found over the deeply reduced sample without the CO_2 multi-prepulse, it can be concluded that CO formation arisen from the re-oxidation of the ceria oxygen vacancies, and that the oxygen species deposited from the CO_2-dissociation were highly reactive for the partial oxidation of the CH_x fragments into the CO product. This partial oxidation process was conceivably based upon the diffusion rate of the surface/subsurface ceria lattice oxygen linked with the oxygen concentration gradient. The CO generation was continuously decreased with the CH_4-pulsing, and almost ceased after the 100 CH_4 pulses. The accumulative quantities of reactive oxygen atoms during the CH_4-pulse was approximately 91.2 μmol, which was comparable to that of the oxygen species deposited from the CO_2-dissociation during the CO_2-prepulse. Significantly, this value is also close to the overall number of the O species formed when the CH_4-pulsing (93.5 μmol) was introduced as soon as the CO_2-prepulse was finished. Thus, these phenomena can safely lead us to deduce that under this operating conditions the desorption of these active oxygen species deposited from the CO_2-dissociation is very slow or hard to occur,

showing that these species are thermally stable instead of the short-living superficial adspecies. All data here combined with the XPS (Fig. S16) and FT-IR (Fig. S15) results strongly indicated that the reactive oxygen adspecies deposited over the surfaces of NiCe-Cav through CO_2-multipulse were actually mostly the atomic species, reactively removable by CH_x species, and reversibly stored. As discussed in Fig. S16, these atomic oxygen was mainly the electrophilic oxygen. Their high reactivity for the CH_4-oxidation and thermo-stability displayed here are in good agreement with the previous reports.[30] It must be pointed out that the oxygen preservation through generation of the CO_2-including superficial adsorbed species (mainly the carbonates) and their following dissociation can be ruled out as the predominantly possible pathway for CO_2-activation on NiCe-Cav because this would result in a ratio value significantly deviating from 1 between the CO formation during CH_4-pulse and the CO_2-consumption during CO_2-pulse, which is not compatible with the results over NiCe-Cav.

3.19 In situ XRD spectra

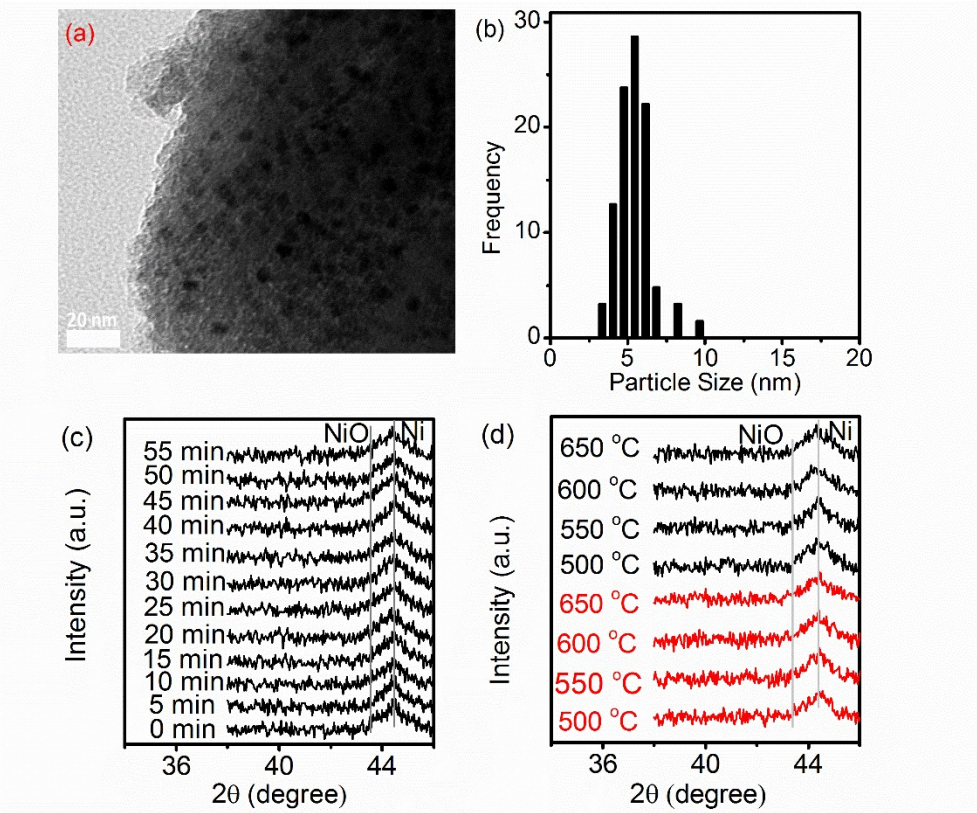

Fig. S19 TEM images (a) and the corresponding Ni NC size distribution (b) of Ni/SiO_2 reduced at 400 °C ;(c) the in situ XRD patterns of the reduced Ni/SiO_2 in the CO_2 flow at 550 °C; (d) the in situ XRD patterns of the NiCe-Cav and NiCe-Vex under the CO_2/CH_4 reforming condition at the different temperatures for 30 min. In Fig.S19 d, the red lines for NiCe-Cav and the black lines for NiCe-Vex.

As well known, SiO_2 are the inert supports, and inactive for the CO_2 activation. Therefore, for comparison, SiO_2 were selected to load the Ni NCs to probe the roles of

the supports in the Ni-NiO transformation. Meanwhile, to exclude effect of the Ni particle size on the Ni-NiO conversion, the Ni/SiO_2 was synthesized as the strategy used for NiCe-Cav and NiCe-Vex, and then reduced at the low temperature of 400 ^oC. As shown in Fig.S19a and S19b, such strategies here led to the Ni NCs with a relatively uniform spread on SiO_2 and a small particle size of 5-6 nm. The Ni particle size of Ni/SiO_2 was similar to that of NiCe-Cav or NiCe-Vex. As clearly seen from Fig.S19c, CO_2 cannot oxidize the Ni NPs in the given contact time and reaction temperature. Given the similar synthetic methods and particle size, the difference in the Ni-NiO conversion between Ni/SiO_2 and Ni/CeO_2 can be ascribed to the disparity in the support properties. In addition, as shown in the main paper, Ni^o on the NiCe-Cav and NiCe-Vex can easily convert into the NiO under CO_2 flow. As well known, the metallic nickel are the active phases for the CO_2/CH_4 reforming, and the oxidation of the metallic nickel can lead to the deactivation of catalysts. To examine whether the oxidation of the metallic nickel into the oxidic nickel occurs under the typical reforming condition and thus contributes to the catalyst deactivation, we inspect the nickel status under the reforming condition at different temperatures. As shown in Fig.S19d, the metallic nickels were not oxidized under typcial CO_2-CH_4 reforming conditions.

5. Supplementary references

1. (a) Q. Yuan, Q. Liu, W. Song, W. Feng, W. Pu, L. Sun, Y. Zhang, C. Yan, *J. Am. Chem. Soc*., 2007, **129**, 6698-6699; (b)W. Zhou, F. Sun, K. Pan, G. Tian, B. Jiang, Z. Ren, C. Tian, H. Fu, *Adv. Fun. Mater*., 2011, **21**, 1922-1930; (c) S. M. Morris, P. F. Fulvio, M. Jaroniec, *J. Am. Chem. Soc.*, 2008, **130**, 15210-15216; (d) X. Tian, T. Xiao, C. Yang, Z. Zhou, H. Ke, *Mater. Chem. Phys*., 2010, **124**, 744-747; (e) T. Brezesinski, M. Antonietti, M. Groenewolt, N. Pinna, B. Smarsly, New J. Chem., 2005, 29, 237-242; (f) P. Hartmann, T. Brezesinski, J. Sann, A. Lotnyk, J. P. Eufinger, L. Kienle, J. Janek, *ACS Nano*, 2013, **7**, 2999-3013; (g) T. Brezesinski, J. Wang, R. Senter, K. Brezesinki, B. Dunn, S. H. Tolbert, *ACS Nano*, 2010, **4**, 967-077; (h) J. Lee, M. C. Orilall, S. C. Warren, M. Kamperman, F. J. DiSalvo, U. Wiesner, *Nat. Mater.*, 2008, **7**, 222-228; (i) Q. Yan, L. Li, S. L. Lu, H. H. Duan, Z. X. Li, Y. X. Zhu, C. H. Yan, *J. Phys. Chem.*, 2009, **113**, 4117-4124; (j) G. Li, D. Zhang, J. C. Yu, *Phys. Chem. Chem. Phys*., 2009, **11**, 3775-3782; (k) W. Cai, J. Yu, C. Anand, A. Vinu, M. Jaroniec, *Chem. Mater*., 2011, **23**, 1147-1157; (l) A. S. Poyraz, C. H. Kuo, S. Biswas, C. K. Kinondu, S. L. Suib, *Nat. Commoun*., 2013, **4**, 2952; (m) D. Li, H. Zhou, T. Honma, *Nat. Mater*., 2004, **3**, 65-72.
2. (a) N. J. Lawrence, J. R. Brewer, L. Wang, T. Wu, J. W. Kingsbury, M.M. Ihrig, G. Wang, Y. L. Soo, W. N. Mei, C. L. Cheng, *Nano Lett*., 2011, **11**, 2666-2671; (b) S. Chang, M. Li, Q. Hua, L. Zhang, Y. Ma, B. Ye, W. Huang, *J. Catal*., 2012, **293**, 195-204; (c) R. Si, M. F. Stephanopoulos, *Angew Chem. Int. Ed*., 2008, **47**, 2884-2887; (d) X. Lu, Y. Zeng, M. Yu, T. Zhai, C. Liang, S. Xie, M. S. Balogun, Y. Tong, *Adv. Mater.*, 2014, **26**, 3148-3155; (e) N. Ta, J. Liu, S. Chenna, P. A. Crozier, Y. Li, A. Chen, W. Shen, *J. Am. Chem. Soc*., 2012, **134**, 20585-20588; (f) P. Gawade, B. Mirkelamoglu,

U. S. Ozkan, J. Phys. Chem. C, 2010, 114, 18173-18181; (Y. Li, W. Shen, *Chem. Soc. Rev*., 2014, **43**, 1543-1574

3. (a) W. Chu., L. N. Wang, P. A. Chenavskii, A. Khodakov, *Angew. Chem. Int. Ed*., 2008, **47**, 5052-5055; (b)F. Guo, W. Chu, H. Xu, T. Zhang, *Chin. J. Catal*., 2007, **28**, 429-434; J. P. Hong, W. Chu, P. A. Chernavskii, A. Y. Khodakov, *J. Catal*., 2010, **273**, 9-17; (c) N. Wang, K. Shen, X. Yu, W. Qian, W. Chu, *Catal. Sci. Technol.*, 2013, **3**, 2278-2287.
4. (a) G. Prieto, J. Zečević, H. Friedrich, K. P. de Jong, P. E. de Jongh, *Nat. Mater.*, 2013, **12**, 34-39; (b) J. R. A. Sietsma, J. D. Meeldijk, J. P. den Breejen, M. V. Helder, A. J. van Dillen, P. E. de Jongh, K. P. de Jong, *Angew. Chem. Int. Ed*., 2007, **46**, 4547-4549; (c) H. Friedrich, J. R. A. Sietsma, P. E. de Jongh, A. J. Verkleij, K. P. de Jong, *J. Am. Chem. Soc.*, 2007, **129**, 10249-10254;
5. (a) T. Odedairo, J. Chen, Z. Zhu, *J. Phys. Chem. C*., 2013, **117**, 21288-21302; (b) J. J. Zhou, C. J. Liu, Y. P. Zhang, *Langmuir*, 2006, **22**, 2334-2339; (c) T. Witvrouwen, S. Paulussen, B. Sels, *Plasma. Processes Polym.*, 2012, **9**, 750-760; (d) P. Shi, C. J. Liu, *Catal. Lett.*, 2009, **133**, 112-118; (d) M. Li, G. Xu, Y. Tian, L. Chen, H. Fu, *J. Phys. Chem. A*, 2004, **108**, 1687-1693; (e) X. Tu, H. J. Gallon, M. V. Twigg, P. A. Gorry, J. C. Whitehead, *J. Phys. D*., 2011, **44**, 274007-274016; (f) G. Bonizzoni, E. Vassallo, Vacuum, 2002, 64, 327-336; (g) X. Zhu, P. Huo, Y. P. Zhang, D. G. Deng, C. J. Liu, *Appl. Catal. B*., 2008, **81**, 132-140.
6. (a) C. Zhang, S. Li, G. Wu, J. Gong, *Catal. Today*, **2014**, *233*, 53-60; (b) T. Odedairo, J. Chen, Z. Zhu, *Catal. Commun.*, **2013**, *31*, 25-31.
7. C. D. Wagner, A.V. Naumkin, A. Kraut-Vass, J. W. Allison, C. J. Powell, J. R. Rumble Jr., NIST X-ray Photoelectron Spectroscopy Database, Version 3.4, National Institute of Standards and Technology, Gaithersburg, MD, **2003**; < http://srdata.nist.gov/xps/ >.
8. (a) M. C. Sánchez-Sanchez, R. M. Navarro, J. L. G. Fierro, *Inter. J. Hydrogen Energy,* **2007**, *32*, 1462-1472; (b) K. Kishi, Y. Hayakawa, K. Fujiwara, *Surf. Sci.*, **1996**, *356*, 171-180.
9. J. F. Moulder, W. F. Stickle, P. E. Sobol, K. D. Bomben, Handbook of X-ray Photoelectron Spectroscopy, Perkin-Elmer Corp. Eden Prairie, Minnesota, USA, **1992**.
10. Y. Zhou, J. Zhou, J. *Phys. Chem. C*, **2012**, *116*, 9544-9546.
11. (a) N. Wang, K. Shen, L. Huang, X. Yu, w. Qian, W. Chu, *ACS Catal.*, **2013**, *3*, 1638-1651; (b) N. Wang, X. Yu, Y. Wang, W. Chu, M. Liu, *Catal Today*, **2012**, *212*, 98-107; (c) N. Wang, Z. Xu, J. Deng, K. Shen, X. Yu, W. Qian, W. Chu, F. Wei, *ChemCatChem*, **2014**, *6*, 1470-1480; (d) L. Xu, H. Song, L. Chou, *Int. J. Hydrogen Energy*, **2012**, *37*, 18001-18020; (e) L. Xu, H. Song, L. Chou, *ACS Catal.*, **2012**, *2*, 1331-1342; (f) N. Sun, X. Wen, F. Wang, W. Wei, Y. Sun, *Energy Environ. Sci*., **2010**, *3*, 366-369; (g) L. Xu, Z. Miao, H. Song, W. Chen, L. Chou, *Catal. Sci., Technol*., **2014**, *4*, 1759-1770.
12. Li C, Yu C, Shen S., *Chin J Catal.*, **2001**, *22*, 377-382.

13. (a) A. E. Galetti, M. F. Gómez, L. A. Arrúa, M. C. Abello, *Appl. Catal. A: Gen.,* **2008**, *348*, 94-102; (b) J. Llorca, N. Homs, J. Sales, J. L. G. Fierro, P. R. dela Piscina, *J. Catal.*, **2004**, *222*, 470-480.
14. F. Tuinstra, J. L. Koenig, *J. Chem. Phys*., **1970**, *53*, 1126-1130.
15. (a) D. O. Hayward, B. M. W. Trapnell, Chemisorption, Second Ed., Butterworths, London, **1964**; R. P. Eischens, W. A. Pliskin, *Adv. Catal.,* **1958**, *10*, 1-56; (c) J. S. Rieck, A. T. Bell, *J. Catal.*, **1987**, *103*, 46-54.
16 (a) R. Razzaq, H. Zhu, L. Jiang, U. Muhammad, C. Li, S. Zhang, *Ind. Eng. Chem. Res.*, **2013**, *52*, 2247-2256; (b) P. A. Redhead, *Trans. Faraday Soc.*, **1961**, *57*, 641-656; (c) J. T. Yates, D. A. King, *Surface Sci.*, **1972**, *30*, 601-616.
17. D. A. Constantiou, A. M. Efstathiou, *Appl. Catal. B*, **2010**, *96*, 276-289.
18. (a) N. Morlanes, Int. J. Hydrogen Energy, 2013, 38, 3588-3596; (b) P. Gruene, A. Fielicke, G. Meijer, D. M. Rayner, Phys. Chem. Chem. Phys., 2008, 10, 6144-6149; (c) H. E. Dorsett, J. E. Reutt-Robey, *Surf. Sci.*, **1997**, *380*, 165-177; (d) S. Morandi, M. Manzoli, F. Prinetto, G. Ghiotti, C. Gerardin, D. Kostadinova, D. Tichit, *Micro. Meso. Mater.*, **2012**, *147*, 178-187; (e) L. Surnev, Z. Xu, J. T. Yates, *Surf. Sci.*, **1988**, *201*, 1-13; (f) J. Lauterbach, M. Wittmann, J. Kuppers, *Surf. Sci.*, **1992**, *279*, 287-296.
19. Z. Hao, Q. Zhu, Z. Jiang, B. Zhou, H. Li, *Fuel Procees. Technol.*, **2009**, **90**, 113-121.
20. P. Marecot, A. Akhachane, J. Barbier, *Catal. Lett.,* **1995**, *36*, 37.
21. (a) S.M. de Lima, A.M. da Silva, L.O. O. da Costa, J. M. Assaf, L.V. Mattos, R. Sarkari, A. Venugopal, F.B. Noronha, *Appl. Catal. B., **2012**, 121/122*, 1–9; (b) F. Pompeo, G.F. Santori, N.N. Nichio, *Catal. Today*, **2011**, *172*, 183-188; (c) L.F. Bobadilla, A. Álvarez, M.I. Domínguez, F. Romero-Sarria, M. A. Cen-teno, M. Montes, J. A. Odriozola, *Appl. Catal. B.,* **2012**, *123/124*, 379-390.
22. D. L. Trimm, *Catal. Rev.*, **1977**, *16*, 155-189.
23. J. H. Edwards, A. M. Maitra, *Fuel. Process Technol*, **1995**, *42*, 269-189.
24. (a) K. Yoon, Y. Yang, P. Lu, D. Wan, H. C. Peng, K. S. Masias, P. T. Fanson, C. T. Campbell, Y. Xia, *Angew. Chem. Int. Ed.*, **2012**, *51*, 9453-9546; (b) Y. Wei, Z. Zhao, J. Liu, C. Xu, G. Jiang, A. Duan, *Small*, **2013**, *9*, 3957-3963; (c) L. D. Rogatis, M. Cargnello, V. Gombac, B. Lorenzut, T. Montini, P. Fornasiero, *ChemSusChem*, **2009**, *3*, 24-42; (d) A. Zhang, B. Xu, X. Wang, *Chem. Soc. Rev*, **2014**, *43*, 7870-7886; (d) K. An, S. Alayoglu, N. Musselwhite, S. Plamthottam, G. Melaet, A. E. Lindeman, G. A. Somorjai, *J. Am. Chem. Soc.*, **2013**, *133*, 16689-16696; (e) J. Shi, *Chem. Rev.*, **2013**, *113*, 2139-2181; (f) T. Schalow, M. Laurin, B. Brandt, S. Schauermann, S. Guimond, H. Kuhlenbeck, D. D. Starr, S. K. Shaikhutdinov, J. Libuda, H. J. Freund, *Angew. Chem. Int. Ed.*, **2005**, *44*, 7601-7605; (g) Q. Fu, F. Yang, X. Bao, *Acc. Chem. Res.*, **2013**, *46*, 1692-1701; (h) I. X. Green, W. Tang, M. Neurock, J. T. Yates, *Acc. Chem. Res.*, **2014**, *47*, 805-815; (i) I. X. Green, W. Tang, M. Neurock, J. T. Y. Jr, *J. Am. Chem. Soc*., **2012**, *134*, 13569-1372; (j) Q. Fu, W. Li, Y. Yao, H. Liu, H. Su, D. Ma, X. Gu, L. Chen, Z. Wang, H. Zhang, B. Wang, X. Bao, *Science*, **2010**, *328*, 1141-1144; (k) G. Chen, Y. Zhao, G. Fu, P. N. Duchesne, L. Gu, Y. Zheng, X. Weng, M. Chen, P. Zheng, C. Pao, J. Lee, N. Zheng, *Science*, **2014**, *344*, 495-499; (l) I. X. Green, W. Tang, M.

Neurock, J. T. Y, Jr, *Science*, **2011**, *333*, 736-739; (m) J. Mannhart, D. G. Schlom, *Science*, **2010**, *327*, 1607-1611.

25. (a) D. Qiao, G. Lu, D. Mao, Y. Guo, Y. Guo, *J. Mater. Sci.,* **2011**, *46*, 641-647; (b) O. Pozdnyakova, D. Teschner, A. Wootsch, J. Kröhnert, B. Steinhauer, H. Sauer, L. Toth, F.C. Jentoft, A. Knop-Gericke, Z. Paál, R. Schlögl, *J. Catal*., **2006**, *237*, 1-16; (c) E.T. Saw, U. Oemar, X. R. Tan, Y. Du, A. Borgna, K. Hidajat, S. Kawi, *J. Catal*., **2014**, *314*, 31-46.

26. (a) K. Sutthiumporn, S. Kawi, *Int. J. Hydrogen Energy*, **2011**, *36*, 14435-14446; (b) K. Sutthiumporn, T. Maneerung, Y. Kathiraser, S. Kawi, *Int. J. Hydrogen Energy,* **2012**, *37*, 11195-11207.

27. (a) M. lwamoto, J. H. Lunsford, *J. Phys. Chem.*, **1980**, *74*, 3079-3084; (b) Y. Osada, S. Koike, T. Fukushima, S. Ogasawara, *Appl. Catal*., **1990**, *59*, 59-74; (c) P. J. Gellings, H. J. M. Bouwmeester, *Catal. Today*, **2000**, *58*, 2-53; (d) M. S. Palmer, M. Neurock, M. M. Olken, *J. Am. Chem. Soc*., **2002**, *124*, 8452-8461.

28. (a) A. A.Khassin, T. M. Yurieva, V. V. Kaichev, V. I. Bukhtiyarov, A. A. Budneva, E. A. Paukshtis, V. N Parmon, *J. Molecular Catal A*., **2001**, *175*, 189-204; (b) G. Chen, B. Han, S. Deng, Y. Wang, Y. Wang, *Electrochimica Acta*, **2014**, *127*, 355-361; (c) C. Weilach, C. Spiel, K. Fottinger, G. Rupprechter, *Surf. Sci*., **2011**, *605*, 1503-1509.

29 (a) J. M. Garcia-Vargas, J. L. Valverde, A. de Luca-Consuergra, B. Gomez-Monedero, P. Sanchez, F. Dorado, *Appl. Catl. A*., **2012**, *431/432*, 49-56; (b) W. Cai, F. Wang, C. Daniel, A. C. van Veen, Y. Schuurman, C. Descorme, H. Provendier, W. Shen, C. Mirodatos, *J. Catal*., **2012**, *286*, 137-152; (c) L. Li, L. Song, H. Wang, C. Chen, Y. She, Y. Zhan, X. Lin, Q. Zheng, *Int. J. Hydrogen Energy*, **2011**, *36*, 8839-8849; (d) Y. He, B. Yang, G. Cheng, *Catal Today*, **2004**, *98*, 595-600; (e) J. M. Garcia-Vargas, J. L. Valverde, F. Dorado, P. Sanchez, *J. Molecular Catal A*., **2014**, *395*, 108-116; (f) W. J. Hong, S. Iwamoto, M. Inoue, *Catal. Today*, **2011**, *164*, 489-494; (g) B. Liu, C. Li, Y. Zhang, Y. Liu, W. Hu, Q. Wang, L. han, J. Zhang, *Appl. Catal. B*., **2012**, *111/112*, 467-475.

30. (a) M. lwamoto, J. H. Lunsford, *J. Phys. Chem*., **1980**, *74*, 3079-3084; (b) Y. Osada, S. Koike, T. Fukushima, S. Ogasawara, *Appl. Catal*., *1990*, **59**, 59-74; (c) P. J. Gellings, H. J. M. Bouwmeester, *Catal. Today*, **2000**, *58*, 2-53; (d) M. S. Palmer, M. Neurock, M. M. Olken, *J. Am. Chem. Soc*., **2002**, *124*, 8452-8461